buildings

MDPI

Article

Research and Development of Steel Fiber Reinforced Concrete Filling Material and Its Application in Gob-Side Entry Retaining Technology in Deep Mines

Xiulong Zhang [1], Xinshuai Shi [1,2,*], Xuehui Li [3,*], Jianguo Ning [1,2], Yuchi Liu [1] and Shang Yang [1]

[1] College of Energy and Mining Engineering, Shandong University of Science and Technology, Qingdao 266590, China; xiulong2022@163.com (X.Z.); njglxh@126.com (J.N.); liu1412837627@163.com (Y.L.); yangshang0214@126.com (S.Y.)
[2] State Key Laboratory of Mining Disaster Prevention and Control Co-Founded by Shandong Province and the Ministry of Science and Technology, Shandong University of Science and Technology, Qingdao 266590, China
[3] College of Transportation, Shandong University of Science and Technology, Qingdao 266590, China
* Correspondence: xs_shi@sdust.edu.cn (X.S.); skd993815@sdust.edu.cn (X.L.)

Abstract: Against the background of the prevailing green development paradigm, numerous coal mines have embraced the adoption of gob-side entry retaining mining technology. The most commonly employed form of gob-side entry retaining involves building an artificial wall along the edge of the goaf behind the working face to maintain the roadway. The pivotal challenge in gob-side entry retaining lies in the roadside support. Currently, commonplace concrete serves as the predominant material for the roadside filling body. Nevertheless, traditional concrete exhibits drawbacks, including inadequate tensile strength and poor toughness, leading to wall cracks or even collapses in the retaining wall. Steel fiber, a frequently employed reinforcement and toughening agent in concrete, has found widespread application in the construction sector and other fields. However, its use as a roadside filling material in underground coal mines remains infrequent. Therefore, in this paper, the flow and mechanical properties of steel fiber concrete were tested and analyzed, and field industrial tests were conducted. Results of indoor experiments show that steel fibers reduce the slump of concrete. The addition of steel fibers shifted the pore compacting stage, linear elasticity stage, and destabilization stage forward and improved the post-peak bearing capacity. The addition of steel fibers makes the concrete compressive and tensile strength show a "first increase and then decrease" trend; both peaked at 1.5%, and the increase in tensile strength is more pronounced. Steel fibers enhance the strength of compressive strength of concrete at an early age, weaker at a late age, and tensile strength inversely. The addition of steel fiber can change the concrete matrix from tensile damage to shear damage, and the toughness index shows the trend of "first increase and then decrease", and reaches the peak value when the dosage is 1.5%. Industrial test results show that steel fiber concrete as a roadside filling body can reduce the surrounding rock surface displacement and bolt (cable) force.

Keywords: filling material; gob-side entry retaining; steel fiber reinforced concrete; surrounding rock control

check for updates

Citation: Zhang, X.; Shi, X.; Li, X.; Ning, J.; Liu, Y.; Yang, S. Research and Development of Steel Fiber Reinforced Concrete Filling Material and Its Application in Gob-Side Entry Retaining Technology in Deep Mines. *Buildings* **2024**, *14*, 722. https://doi.org/10.3390/buildings14030722

Academic Editor: Guozhu Zhang

Received: 24 January 2024
Revised: 4 March 2024
Accepted: 6 March 2024
Published: 7 March 2024

Copyright: © 2024 by the authors. Licensee MDPI, Basel, Switzerland. This article is an open access article distributed under the terms and conditions of the Creative Commons Attribution (CC BY) license (https://creativecommons.org/licenses/by/4.0/).

1. Introduction

Coal is a pivotal energy resource in China, providing essential support for the robust development of the nation's economy. Presently, the majority of China's coal extraction occurs underground, with numerous adhering to the practice of preserving coal pillars for the exploitation of working faces [1]. A coal pillar (Figure 1a), established temporarily or left unexplored in subterranean coal mines used to separate the gob entry and the gob area of the previous panel, is a measure taken to guarantee the mine's safe production [2]. However, the persistence of the coal pillar exacerbates the loss of coal resources. To mitigate the loss

of coal resources and align with the principles of green mining [3,4], numerous mines have embraced the implementation of gob-side entry retaining technology [5,6]. Gob-side entry retaining (GER) diligently upholds the roadway, delineating the gob boundary behind the working face. The primary thoroughfare is conscientiously conserved and repurposed as an adjacent roadway to the working face, facilitated by the adept application of efficient roadside backfill and road-in support technology [7]. Currently, the most commonly employed form of gob-side entry retaining involves constructing an artificial wall along the edge of the goaf behind the working face to maintain the roadway, as shown in Figure 1b. The substitution of artificial walls for the original coal pillars has increased the coal resource recovery rate and enhanced the efficiency of roadway excavation. Furthermore, it has the capacity to reduce the stress concentration on coal pillars, rendering it advantageous for the working face of high-gas mines [2,8]. The key to gob-side entry retaining is the roadside support. The current gob-side entry retaining mostly uses ordinary concrete as the roadside filling material, while traditional concrete is a brittle material with low tensile strength, poor toughness, and other shortcomings [9]. As coal mining depth intensifies, the roadside backfill body grapples with the challenges of the "three tenors one disturbance" geological mechanics environment, and the extant backfill materials prove insufficient in completely satisfying the demands of secure production [10,11]. Consequently, the roadside backfill body frequently experiences destabilization and damage [12], impinging upon the mine's safe production. Hence, the research and development of new high-strength, high-toughness roadside filling materials has become an inevitable trend.

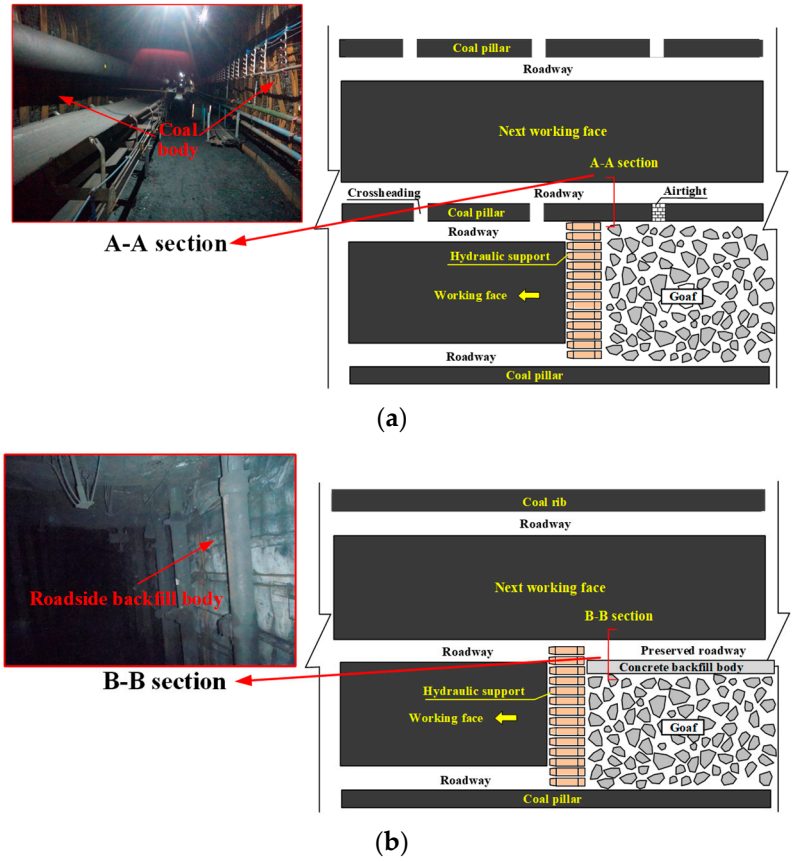


Figure 1. Comparison of mining methods (Plan view): (**a**) leave a coal pillar mining; (**b**) mining of gob-side entry retaining.

With the aim of enhancing the toughness and durability of concrete, endeavors have been undertaken to augment concrete through the incorporation of unconventional materials, including fibers [13–15], rubber particles [16–18], carbon nanotubes [19–22], and

ceramics [23–25]. Several studies have demonstrated that the addition of steel fibers can substantially enhance the strength and toughness of the concrete matrix [26–31]. Steel fiber has become a popular modification material due to its competitive pricing, easy access to raw materials, and other advantages. Scholars have extensively investigated the reinforcing effect of steel fiber on concrete from various perspectives. For instance, Wang et al. [32] investigated the impact of various steel fiber admixtures on the mechanical properties of concrete. The study found that the mechanical properties of steel fiber concrete exhibited a trend of initially increasing, then decreasing, and ultimately peaking at a 2% admixture. Meng et al. [33] studied the impact of steel fiber distribution on flexural properties. Their findings revealed a quadratic correlation between the fiber orientation coefficient and the number of fiber pull-outs. Luo et al. [34] proposed a new mechanical model for the microfracture zone at the crack tip during the fracture of SFRC based on the effective modulus of elasticity and considering the sidewall effect and gravity effect. Sun et al. [35] investigated the interfacial bond strength from a microscopic perspective, examining the effects of fiber shape and diameter. The study found that variations in fiber diameter and embedment depth did not significantly impact interfacial bond strength, whereas changes in fiber profile had a significant effect. In contrast, Rashidi's [36] research focused on the impact of steel fibers on concrete fracture energy through numerical simulation.

Steel fiber reinforced concrete (SFRC) is a commonly used material in highways, tunnels, and construction [37–39]. However, its use as underground roadside filling material has not been extensively studied. Therefore, this paper takes SFRC as underground roadside filling material as the research theme, adopts the research method of combining indoor experiments and on-site practice, and, for the first time, applies SFRC to underground roadside filling material for use. First, the slump degree of SFRC with different steel fiber dosages was measured to test whether its fluidity meets the actual requirements of the project. The specimens of SFRC with different curing ages and different steel fiber dosages were prepared, and their mechanical properties were tested to analyze the reinforcing and toughening effect of steel fibers. Finally, the on-site engineering application was carried out in a coal mine in Shanxi, and the effect of the surrounding rock control was monitored, which provided valuable experience for solving similar problems in the future.

2. Materials and Methods

2.1. Specimen Preparation

The cementitious material employed in this experiment is ordinary Portland cement (po42.5), with its primary parameters detailed in Table 1. The coarse aggregate comprises gangue obtained from mine excavations. In adherence to the regulations outlined in DG/TJ 08-59-2019 (Chinese standards) [40], the maximum particle size must not exceed 20 mm. Therefore, this experiment utilizes 5~20 mm continuous graded gravel, possessing an apparent density of 2680 kg/m^3, and according to the stacking experiment, the mixing ratio of crushed stones with two particle sizes of 5 mm~10 mm and 10 mm~20 mm is determined to be 2.5:7.5, with its primary parameters detailed in Table 2. The fine aggregate consists of medium-grained sand with a particle size ranging from 0.25 mm to 0.5 mm, a fineness modulus of 2.7, mud content less than 1%, and an apparent density of 2360 kg/m^3, with its primary parameters detailed in Table 3. The steel fiber employed is of the milling wave shape, with specific parameters detailed in Table 4. The water reducer used is a polycarboxylate superplasticizer, exhibiting a water reduction rate exceeding 25%, with its primary parameters detailed in Table 5. The experimental water utilized is laboratory tap water.

Table 1. Cement composition (%).

Parameter	MgO	SiO_2	Al_2O_3	CaO	Fe_2O_3	Na_2O	K_2O	Others	Loss
Index	3.1	24	8.5	43.4	2.6	0.29	0.7	0.8	16.61

Table 2. Main components of coarse aggregate (%).

Parameter	MgO	SiO_2	Al_2O_3	CaO	Fe_2O_3	SO_3	FeO	Loss
Index	7.1	54.3	16.2	10.4	6.5	0	5.5	0

Table 3. Main components of fine aggregate (%).

Parameter	SiO_2	Fe_2O_3	Other	Moisture Content
Index	98.5	0.02	1.48	1.5

Table 4. Main parameters of milling steel fiber.

Parameter	Tensile Strength	Length	Width	Thickness	Density
Index	680 Mpa	38 mm	2 mm	0.5 mm	7.8 kg/m^3

Table 5. Main parameters of water reducing agent.

Parameter	Water Reduction	Gas Holdup	Bleeding Rate	Water Content	PH Value
Index	≥25%	≤6.0%	≤60%	≤3%	7.0 ± 1.0

First, prepare various materials required for the experiment and wet tools such as shovels. Then, weigh the required amount of materials for each mix ratio and stir. After mixing, brush mineral oil inside the mold, then add concrete in two batches and compact it with a tamping rod. After filling the mold with concrete, grind the surface of the trial mold flat and place it on a vibration table to shake out the bubbles. Finally, seal the trial mold with cling film and place it in the curing room for maintenance. The flow of experimental raw materials and specimen fabrication is shown in Figure 2.

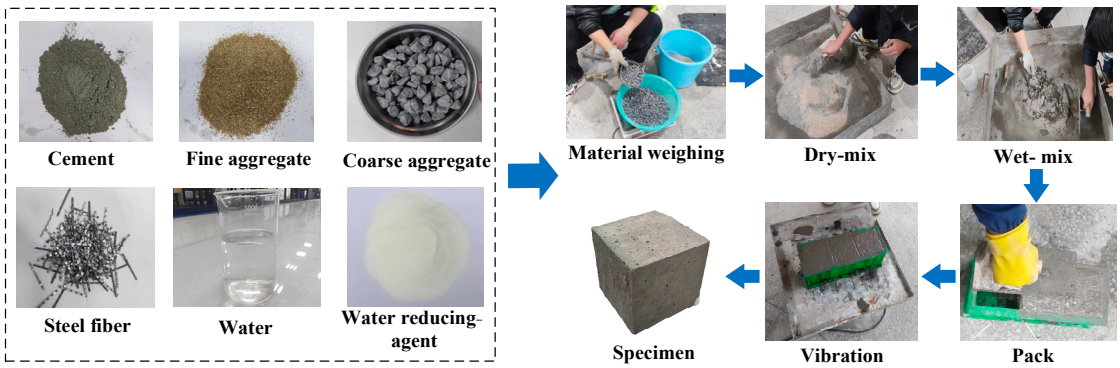


Figure 2. The flow of experimental raw materials and specimen fabrication.

According to JGJ55-2011 (Chinese standards) [41] regulations, the absolute volumetric method is used to calculate the basic mixing ratio of C40 ordinary concrete. On the basis of this ratio, the amount of steel fiber is calculated according to the assumed mass method in the standard JG/T472-2015 (Chinese specification) [42]. The design admixture of steel fiber ranges from 0 to 2%, increasing by 0.5% in each gradient [43–45]. The water–cement ratio remained constant throughout the experiment, and the amount of water-reducing agent was determined to be 0.3% of the cement dosage. The experimental number of ordinary concrete is set to C, and the experimental number of SFRC is set to SFRC-X, for example, SFRC-5, which indicates that the steel fiber admixture is 0.5%, and so on. The experimental mixing ratios are shown in Table 6.

Table 6. Experimental mix proportion.

Experiment Number	Cement (kg/m^3).	Coarse Aggregate (kg/m^3).	Fine Aggregate (kg/m^3).	Steel Fiber (kg/m^3).	Water (kg/m^3).	Water Reducer (kg/m^3).
C	382.6	920	830	0	176	1.14
SFRC-5	382.6	910	840	39.25	176	1.14
SFRC-10	382.6	875	875	78.5	176	1.14
SFRC-15	382.6	840	910	117.5	176	1.14
SFRC-20	382.6	805	945	157	176	1.14

2.2. Test Contents

2.2.1. Determination of Slump

In the construction of gob-side entry retaining, the grout has to be transported to the site through the grout pipe. Therefore, the fluidity of the grout is also a factor to be considered during field construction, and fluidity is usually reflected in the collapse of the freshly mixed concrete. For this reason, SFRC collapse measurements are required, and the slump experiment was carried out according to the standard GB/T 50080-2016 [46] (Chinese standard, International standards can refer to ASTM-C143 [47]). Firstly, clean the inside and outside of the slump cylinder thoroughly. Then, divide the concrete into three parts, add it to the slump cylinder, and evenly insert it with a tamping rod. After the top layer is compacted, remove any excess concrete. Finally, lift the slump cylinder vertically and measure the difference between the highest point of the concrete and the highest point of the slump cylinder, which is the slump.

2.2.2. Determination of Mechanical Properties Parameters

After the excavation of the working face, the overlying roof will gradually sink with time, and the overlying load of the backfill body will also be different at different times. In order to meet the actual situation of the engineering site, this article mainly determines the compressive strength and splitting tensile strength of the cube when the curing age is 3 days, 7 days, and 28 days. To eliminate some degree of variation, three samples were taken for each age and proportion, totaling 90 specimens. According to the GB/T 50081-2019 standard [48] (Chinese standard), the compressive strength (International standards can refer to ASTM-C39 [49]) and tensile strength (International standards can refer to ASTM-C496 [50]) are both 100 × 100 × 100 mm non-standard size specimens. Among them, the strength conversion coefficient of non-standard specimens in the cube compression test is 0.9, and the strength conversion coefficient of the cube splitting tensile test is 0.8. The cube-splitting tensile test requires the use of specified fixtures and the use of specified cushion blocks and strips before the experiment can be conducted. The hardening temperature of the specimen is maintained at 20 ± 2 °C, and the relative humidity is maintained at ≥95%.

The experiment was conducted on the SHT4605 electronic universal testing machine at Shandong University of Science and Technology. The SFRC specimens were loaded using a controlled force loading method, with a loading rate of 0.5 MPa/s for the cube compression test and 0.05 MPa/s for the splitting tensile test. The experimental test sequence is shown in Figure 3.

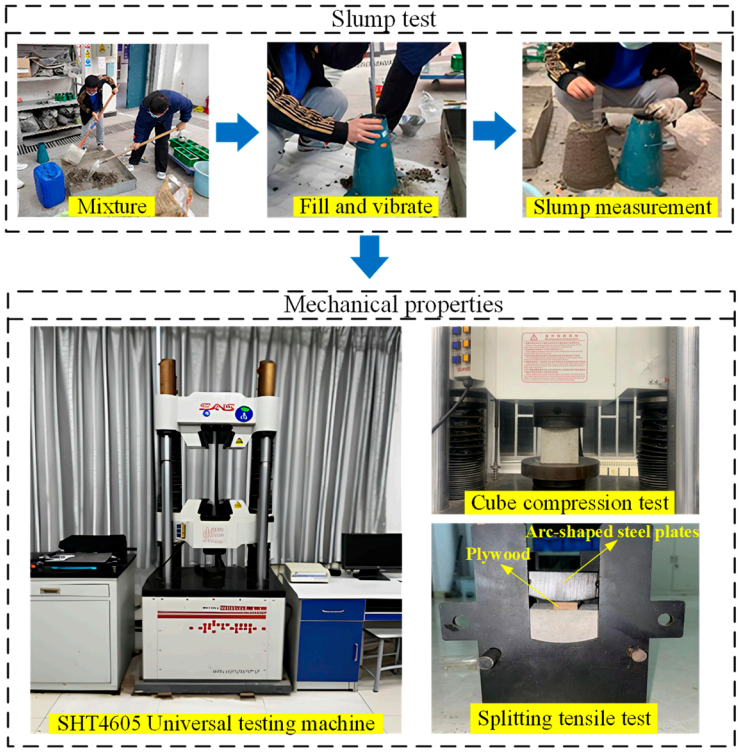


Figure 3. The experimental test flow.

3. Results and Analysis

3.1. Analysis of Slump Results

The slump test results of concrete with different steel fiber contents are shown in Figure 4a. From Figure 4a, it can be seen that the slump values of SFRC-5, SFRC-10, SFRC-15, and SFRC-20 were 148 mm, 130 mm, 113 mm, 105 mm, and 75 mm, respectively. The slumps were reduced by 12%, 23%, 29%, and 75%, respectively, when compared with normal concrete (Group C). The slump value of the concrete gradually decreased with the increase of steel fiber admixture, and the fluidity became poor; the steel fiber dosage of 2% is only 75 mm, which does not meet the pumping requirements. The analysis suggests that the steel fibers will overlap each other inside the concrete to form a steel fiber network. As the amount of admixture increases, the moving space of the steel fibers in the slurry gradually decreases, which increases the resistance to slurry flow and thus reduces slump [51]. The steel fiber used in the experiments of this paper is more slender compared to the coarse aggregate, and the specific surface area is larger under the same volume condition, which increases the friction between the aggregate and the fiber. When the steel fiber content is more, there will be uneven mixing to bring the fibers together, forming fiber clusters, reducing the slump of the concrete, and making the slurry liquidity worse [52].

In actual on-site construction, the concrete preparation and conveying unit is arranged in the connecting roadway, but there is a certain distance between the connecting alley and the construction site. To determine the maximum pumping distance of SFRC under different ratios, the maximum pumping distance of SFRC under different ratios is calculated according to the provisions of JGJ/T 10-2011 (Chinese standard) [53]. The calculation formula is shown in Equations (1)–(3).

$$v = \frac{Q}{3600\pi r^2} \tag{1}$$

where v is the flow velocity of concrete inside the horizontal pipe, m/s; Q is the conveying capacity of the concrete pump, m^3/h; r is the radius of the conveying pipeline, m.

$$\Delta P_H = \frac{2}{r}\left[k_1 + k_2\left(1 + \frac{t_2}{t_1}\right)v\right]\alpha_1 \quad (2)$$

where ΔP_H is the pressure loss per meter of horizontal pipeline, Pa/m; v is the concrete flow velocity inside the horizontal pipe, m/s; r is the pipeline radius of the conveying pipe, m; K_1 is the adhesion coefficient, $K_1 = (3.0 - 0.1S_1) \times 100$, Pa; K_2 is the velocity coefficient, $K_2 = (4.0 - 0.1S_1) \times 100$, Pa/m/s; t_2/t_1 is ratio of concrete pump dispensing valve switching time to piston push concrete time, Take 0.3 temporarily; S_1 is the slump of fresh concrete, in cm; α_1 is the ratio of lateral pressure to axial pressure of concrete, Take 0.9 temporarily.

$$L_{\max} = \frac{P_C - P_1}{\Delta P_H} \quad (3)$$

where L_{max} is the maximum horizontal distance of concrete pumping, m; Pc is rated working pressure of concrete pump, MPa; P_1 is the internal pressure loss of the concrete pumping system MPa, it is generally ignored and taken as 0; ΔP_H is the pressure loss per meter of concrete flowing in the horizontal conveying pipe, Pa/m.

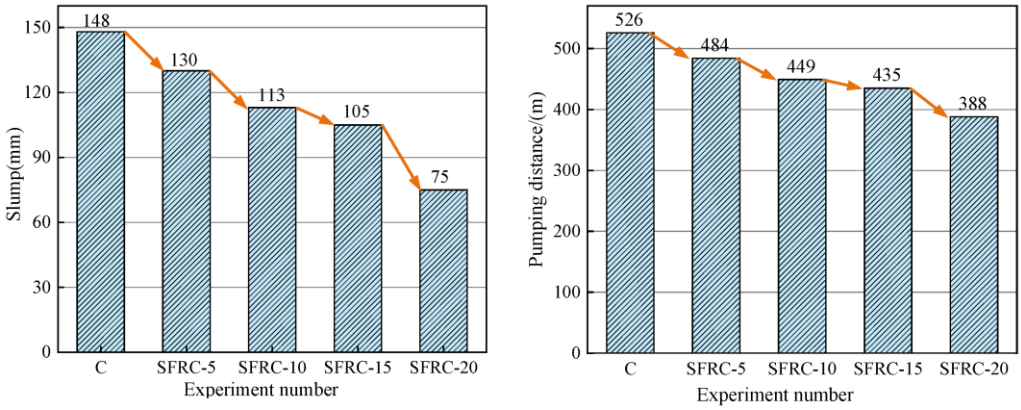


Figure 4. Collapse and maximum pumping distance: (**a**) slump; (**b**) maximum pumping distance.

The current pump pressure used in this mine is 7.4 MPa, with a pumping capacity of 40 m^3/h and a pipe diameter of 0.125 m. The pumping distance is calculated by substituting the above parameters into Formulas (1)–(3), and the results are shown in Figure 4b. Taking into account the calculation results of slump and maximum pumping distance, as well as factors such as concrete and workability, the actual amount of steel fiber added during on-site construction should be between 0.5% and 1.5%.

3.2. Characteristics of Stress–Strain Curve in Cube Compression Test

Figure 5 shows the stress–strain curves and typical stress–strain curves of SFRC at different curing ages. Since the stress–strain curves of SFRC at different curing ages show approximately the same pattern, this paper illustrates the stress–strain curves of SFRC at a curing age of 28 days.

From Figure 5a, it can be seen that, similar to the stress–strain curve of ordinary concrete, the stress–strain curve of SFRC specimens can also be divided into Pore compaction stage (OA stage), linear elasticity stage (AB stage), instability failure stage (BC stage), and post-peak residual stage (CD stage) [54].

Pore compaction stage (OA stage): due to the presence of natural defects such as pores in concrete, they will be compacted under compressive loads, resulting in an increase in slope on the stress–strain curve. From Figure 5b–d, it can be seen that when the amount of steel fiber added changes from 0.5% to 1.5%, the slope of the pore compaction stage gradually increases and enters the linear elastic stage faster.

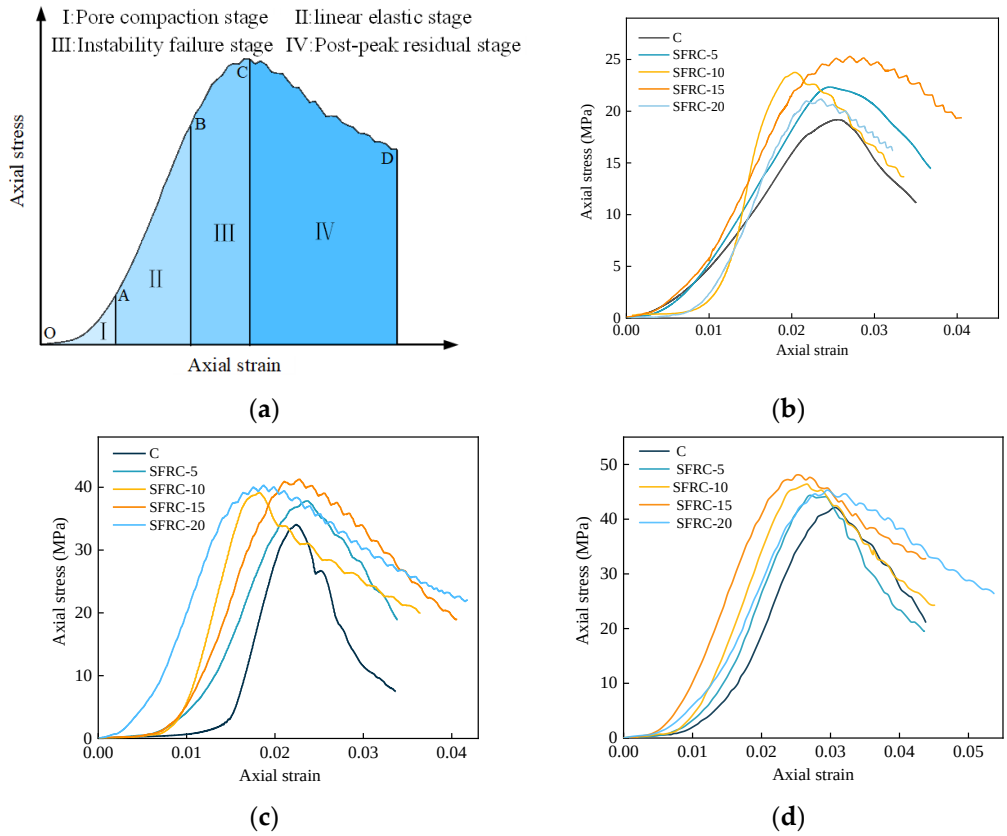


Figure 5. Stress–strain curve of SFRC: (**a**) Typical stress–strain curve; (**b**) 3–day stress–strain curve; (**c**) 7–day stress–strain curve; (**d**) 28–day stress–strain curve.

Linear elasticity stage (AB stage): during this stage, the stress–strain curve is approximately a straight line, with the slope basically unchanged. As the axial load increases, the deformation of the specimen gradually increases, and the slope gradually increases with the increase of steel fiber content.

Instability failure stage (BC stage): in this stage, the specimen has reached the yield load and entered the plastic failure stage from the linear elastic stage. The stress–strain curve shows an upward convex phenomenon, and the slope of the curve gradually decreases. The internal cracks of the specimen develop rapidly, causing the specimen to fail.

Post-peak residual stage (CD stage): from Figure 5b–d, it can be seen that when ordinary concrete (Group C) reaches its peak load capacity, its compressive strength will suddenly decrease and lose its bearing capacity. When SFRC reaches its peak load capacity, its compressive strength does not experience a sudden decrease, but shows a stepwise downward trend with the increase of strain, and the post peak bearing capacity becomes stronger.

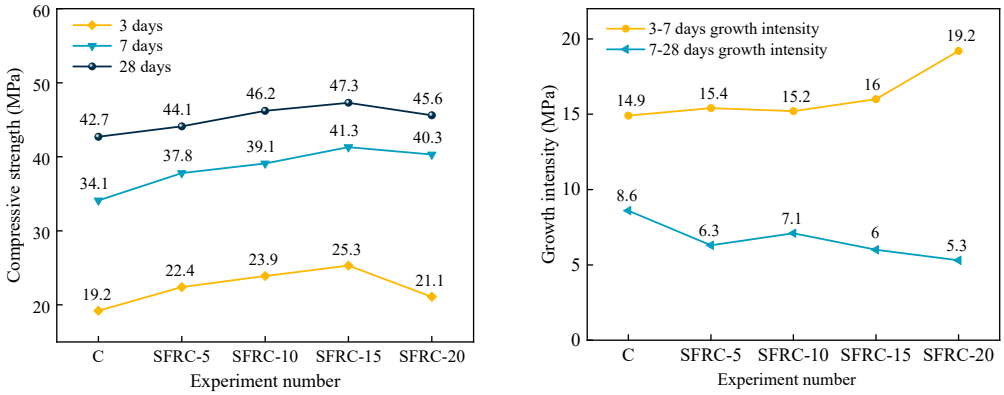
3.3. Development Law of Strength of SFRC

3.3.1. Development Law of Cube Compressive Strength

Compressive strength test results are shown in Table 7 (in conversion). In order to analyze the strength growth law of SFRC, the average value of cubic compressive strength of SFRC with different admixtures and ages are shown in Table 7, and the strength growth between different admixtures and ages were plotted as curves as shown in Figure 6.

Table 7. Compressive strength test results/MPa.

Experiment Number			C	SFRC-5	SFRC-10	SFRC-15	SFRC-20
conservation age	3 days	Specimen 1	20.1	21.9	25.3	27.6	19.6
		Specimen 2	18.9	22.4	23.0	24.7	20.9
		Specimen 3	18.6	22.9	23.4	23.9	22.8
		average	19.2	22.4	23.9	25.3	21.1
	7 days	Specimen 1	34.9	36.8	40.0	40.8	42.1
		Specimen 2	32.8	38.4	38.7	41.2	37.8
		Specimen 3	34.6	38.2	38.6	41.3	41.0
		average	34.1	37.8	39.1	41.1	40.3
	28 days	Specimen 1	44.7	42.6	48.6	45.8	45.4
		Specimen 2	43.0	44.5	47.2	48.3	47.0
		Specimen 3	40.4	45.2	42.8	47.8	44.4
		average	42.7	44.1	46.2	47.3	45.6



(**a**) (**b**)

Figure 6. Experimental data of cube compressive: (**a**) compressive strength; (**b**) growth intensity between different maintenance ages.

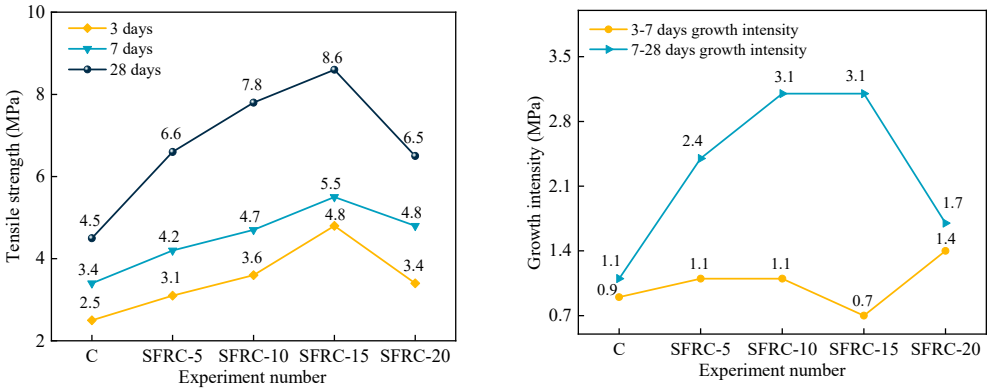
As shown in Figure 6a, with the increase of steel fiber content, the cubic compressive strength of SFRC shows a trend of first increasing and then decreasing, but the growth rate is relatively small. When the steel fiber content is between 0.5% and 1.5%, the compressive strength of the cube shows a linear growth trend. However, when the steel fiber content is 2%, the compressive strength of the cube is lower than that of the cube when the content is 1.5%. As shown in Figure 6b, when the curing age is from 3 to 7 days, the growth strength shows an upward trend with the increase of steel fiber content. When the maintenance period is from 7 to 28 days, the growth strength shows a decreasing trend with the increase of steel fiber content. From this, it can be seen that the addition of steel fibers has a strong effect on improving the early compressive strength of concrete and a relatively small effect on improving the later compressive strength.

3.3.2. Development Law of Splitting Tensile Strength

The tensile strength test results are shown in Table 8 (in conversion). The average values of tensile strength of SFRC with different admixtures and ages in Table 8 were plotted as curves with the increase in strength between different admixtures and ages, as shown in Figure 7.

Table 8. Tensile test results/MPa.

Experiment Number			C	SFRC-5	SFRC-10	SFRC-15	SFRC-20
conservation age	3 days	Specimen 1	2.4	3.5	4.0	4.7	3.9
		Specimen 2	2.1	2.9	3.7	4.8	2.3
		Specimen 3	3.0	2.9	3.1	4.9	4.0
		average	2.5	3.1	3.6	4.8	3.4
	7 days	Specimen 1	3.9	4.1	5.1	5.0	4.7
		Specimen 2	3.7	4.3	4.8	6.1	4.2
		Specimen 3	2.6	4.2	4.2	4.9	5.5
		average	3.4	4.2	4.7	5.5	4.8
	28 days	Specimen 1	4.3	6.7	7.8	8.4	6.4
		Specimen 2	5.2	7.0	8.1	8.8	7.1
		Specimen 3	4.0	6.1	7.5	8.6	6.0
		average	4.5	6.6	7.8	8.6	6.5



(**a**) (**b**)

Figure 7. Experimental data of splitting tensile strength: (**a**) split tensile strength; (**b**) growth intensity between different maintenance ages.

According to Figure 7a, it can be seen that the tensile strength shows a trend of first increasing and then decreasing with the increase of steel fiber content, which is consistent with the pattern shown in the cube compression test. The significant improvement in tensile strength is similar to the findings of the studies by Bai et al. [55] and S.H. et al. [56]. There is a critical value for the amount of steel fibers added. When the amount exceeds the critical value, it will reduce the workability of concrete, resulting in uneven distribution of steel fibers in the concrete matrix and agglomeration, as shown in Figure 8, which affects the quality of hardened concrete and reduces its compressive and tensile strength.

From Figure 7b, it can be seen that with the increase of steel fiber content, the increase in strength is relatively small when the curing age is from 3 to 7 days, and it shows a trend of "rise decrease rise"; when the maintenance period is from 7 to 28 days, the intensity growth rate increases significantly, showing a trend of first increasing and then decreasing. From this, it can be seen that steel fibers have a relatively small effect on improving the early splitting tensile strength of concrete but a greater effect on improving the later splitting tensile strength.

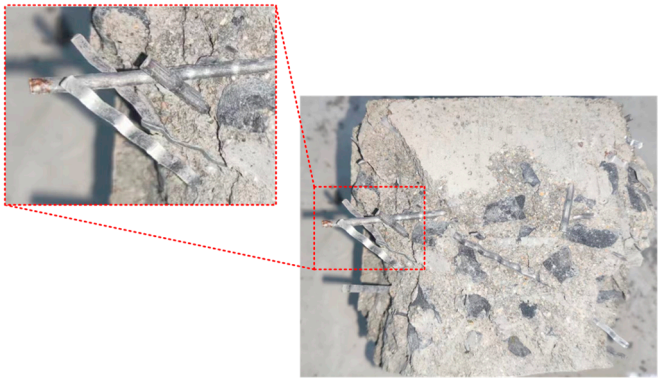


Figure 8. Steel fiber aggregation.

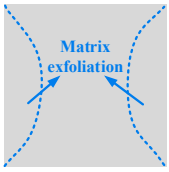
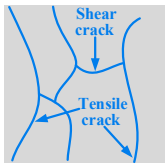
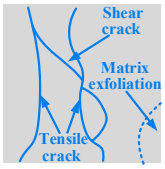
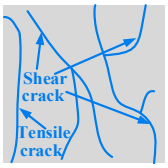
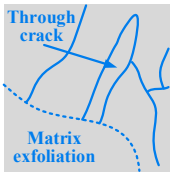
3.4. Specimen Damage Pattern

Due to the similar failure patterns of SFRC specimens with different curing ages, the failure modes of SFRC specimens with a curing age of 28 days are explained in this study.

3.4.1. Damage Morphology of Cube Compression Test

Table 9 shows the damage morphology of the experimental specimens of steel fiber concrete cubic compression tests with different admixtures at a curing age of 28 days.

Table 9. Cube compression test damage pattern.

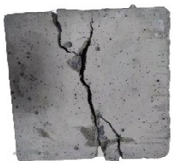
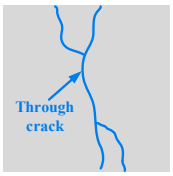
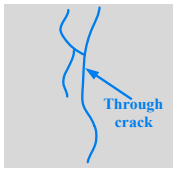
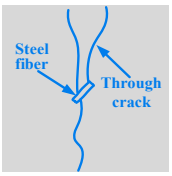
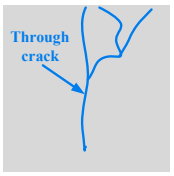
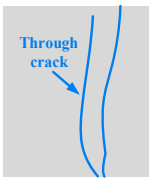
Number	C	SFRC-5	SFRC-10	SFRC-15	SFRC-20
Real shot image					
Sketch Map					

According to Table 9, it can be seen that the ordinary concrete (Group C) specimen suffered severe damage during the experiment, with tension cracks generated by loading penetrating the entire specimen. The concrete matrix on both sides of the specimen was peeled off, resulting in an X-shaped cross-failure pattern, which is a typical brittle failure. With the increase of steel fiber content, the degree of damage to the failure surface gradually decreases, and the tensile cracks gradually decrease while the shear cracks gradually increase. The failure mode of the specimen transitions from tensile failure to shear failure [57], with relatively good integrity. But when the steel fiber content is 2%, there is a lot of block peeling phenomenon in the concrete matrix, and through cracks are formed on the surface of the specimen, resulting in a large degree of damage to the specimen.

3.4.2. Damage Morphology Analysis of Splitting Tensile Test

Table 10 shows the damage morphology of split tensile test specimens of concrete with different steel fiber admixtures at a curing age of 28 days.

Table 10. Splitting tensile strength damage pattern.

Number	C	SFRC-5	SFRC-10	SFRC-15	SFRC-20
Real shot image					
Sketch Map					

As shown in Table 10, when the load borne by ordinary concrete (Group C) reaches its ultimate tensile strength, a crack with the same loading direction will quickly form, and the specimen will be split into two independent parts, resulting in poor integrity of the specimen. As the amount of steel fiber added increases, the crack width formed during the loading of the specimen gradually decreases, and the concrete specimen with steel fiber added can still remain as a whole after failure, with good integrity. But when the amount of steel fiber added is 2%, the through cracks formed under load shift, and the resulting crack width is larger.

3.5. The Toughening Effect of Steel Fibers

Toughness refers to the ability of a material to continue to resist loading and to deform continuously after undergoing plastic deformation under external forces. It can usually be expressed as the ratio of the energy [58,59] absorbed by the material to its volume, and the energy can be calculated using the methods in references [58,59]. The Toughening Index of steel fibers at a curing age of 28 days is now calculated using Formula (4), as shown in Figure 9.

$$R = \frac{E}{V} \tag{4}$$

where R is the toughness index, J/cm^{-3}; E is the energy absorbed by the specimen, J; V is the volume of the specimen, cm^3.

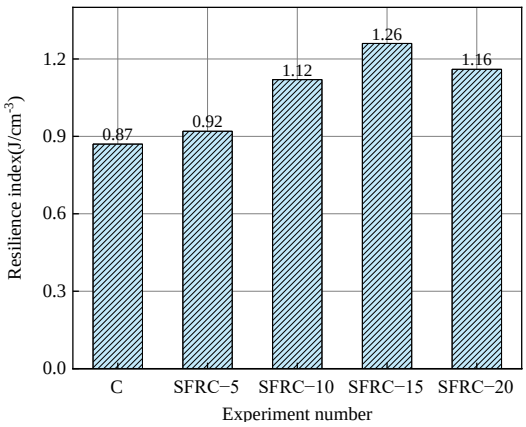


Figure 9. Toughness index of different steel fiber content.

From Figure 9, it can be seen that the toughening index follows the same pattern as the cube compression test and splitting tensile test, both showing a trend of "increasing first and then decreasing". Among them, when the steel fiber content is 1.5%, its toughness

index is the highest, the suction effect is the best, and the resistance to deformation is the strongest. It is analyzed that when the specimen is loaded, the load is transferred from the concrete matrix to the steel fibers, and due to the fact that the elastic model of the steel fibers themselves is much larger than the Young's modulus of the concrete matrix, it can slow down the degree of increase of load in the concrete matrix, which in turn improves the resistance to deformation of the concrete matrix, and increases the toughness of the concrete matrix [60]. It can also be seen from the stress–strain curves in Section 3.2 of the paper that the addition of steel fibers makes the Young's modulus of the concrete matrix larger, and the stress–strain curves are more full of points after the peak. In addition, the type of steel fibers used in this paper are molded steel fibers. According to research, shaped steel fibers have a larger contact area with the concrete matrix and bite into the concrete matrix to form a mechanical bite force. This increases the work done by external loads and increases the energy absorbed by the concrete matrix, which in turn increases the toughness of the concrete matrix [61,62].

4. Industrial Testing

Based on the previous research results, it can be concluded that a steel fiber content of 1.5% achieves the best performance. When the curing age is 28 days, the compressive strength is 47.3 MPa, the tensile strength is 8.6 MPa, and the toughness index is 1.26 J/cm^{-3}, which is 10%, 91%, and 44% higher than ordinary concrete, respectively. Moreover, the integrity of the specimens is the best after failure. The slump is 105 mm, which meets the requirements for concrete pumping. In order to test the effectiveness of SFRC-filled wall support, this article conducted on-site industrial tests in a coal mine in Shanxi.

4.1. Experimental Site and Backfill Body Design

Through on-site investigation, it is known that the concrete preparation unit is currently arranged in the 5# connection roadway. Although it was theoretically calculated in Section 3.1 that the maximum conveying distance for steel fiber with a content of 1.5% is 435 m, in order to avoid problems such as pipe blockage, the experiment was conducted in the N1306 transportation roadway at a distance of 100–150 m from the 5# connecting roadway. The specific location is shown in Figure 10. A comprehensive examination of the results of indoor experiments and site construction conditions showed the actual construction of steel fiber blending amount of 1.5%, with the water–cement ratio and experiments to maintain the same, but the use of cement grade changed to po32.5. Other materials and indoor experiments used the same materials, but taking into account the construction time, coarse aggregate did not carry out the design of continuous grading. The mine is now using the flexible mold concrete stay-along technology, a single flexible mold package dimensions of 5.0 m × 1.5 m × 3.6 m (length × width × height), then each flexible mold package needs to add about 2 tons of steel fiber. The support method in the alley remains unchanged, and parameters such as the amount of steel fiber added and the size of the filling wall can be gradually changed according to the actual support effect to reduce costs.

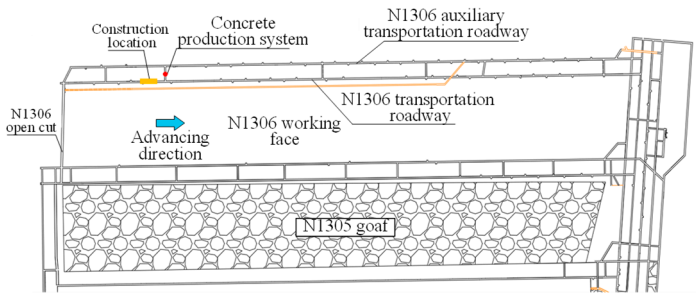


Figure 10. Test implementation site.

4.2. Construction Equipment and Technology

4.2.1. Construction Equipment

The mine adopts the KTRHZSJ-50 flexible formwork concrete preparation and conveying unit, which consists of two parts: concrete mixer and scraper feeder. The concrete mixer model is MJSY-2300G, with a nominal capacity of 2300 L, a production capacity of 50 m^3/h, a maximum aggregate particle size of 20 mm, a rated voltage of 660/1140 V, and a motor power of 55 kW. The scraper feeding machine model is GYG420-12.7, with a feeding section length of 20 m, a production capacity of 50 m^3/h, an aggregate particle size of 20 mm, a voltage of 660/1140 V, and a motor power of 55 kW.

4.2.2. Construction Technology

Firstly, transport the ground filling material to the temporary underground material yard to prepare for the pouring of the filling body. Spread cement, coarse aggregate, fine aggregate, and steel fiber evenly at the mixing site, and then use a forklift to mix the spread dry material evenly. After mixing, turn on the scraper machine and use a forklift to transport the mixed materials to the scraper feeder. The scraper feeder transports the materials to the mixing bin and adds water for mixing to form a pumped slurry. After the mixing is completed, the conveying pump is turned on to provide pump pressure to the pipeline. The slurry is pumped through the pipeline to the pouring site of the filling body for pumping. The construction equipment and process are shown in Figure 11.

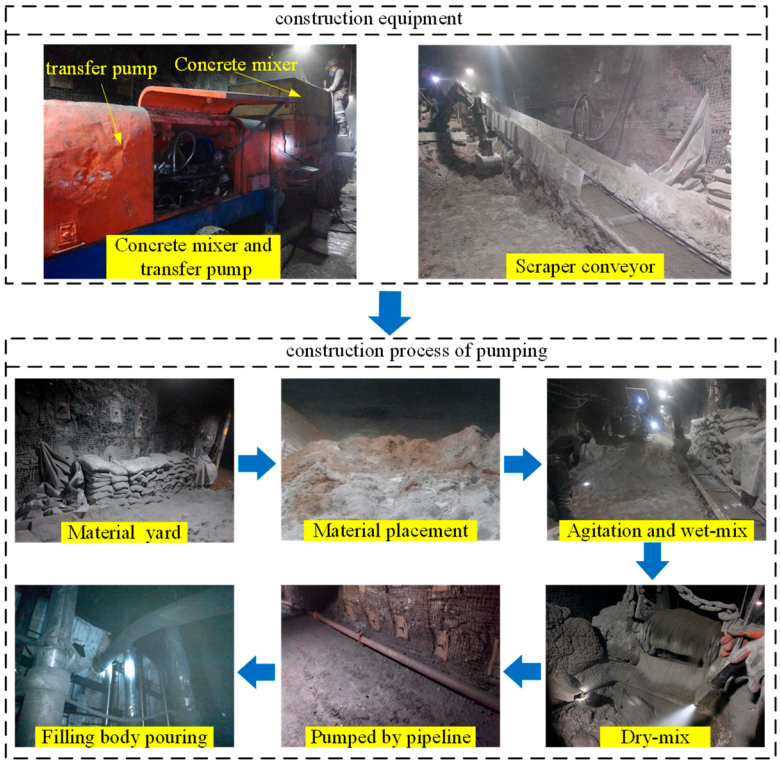


Figure 11. Construction process of pumping.

4.3. Implementation Effect Monitoring

4.3.1. Monitoring Content

This time, we mainly monitor the displacement of the roadway surface and the force of the bolt (cable); among them, the section of the N1306 transportation roadway is rectangular, and the size of the roadway is 5.2 m × 3.6 m (width × height). Six bolts and three cables are installed on the top plate of the roadway, of which the row spacing between the bolts is 0.9 × 1.0 m and that between the cables is 1.6 × 3.0 m; four bolts are installed on the left gang of the roadway, of which the row spacing between them is 1.0 × 1.0 m, and six bolts

are installed on the backfill body with a row spacing of 0.6 × 1.0 m. Set up Station 1 in the ordinary concrete construction area and Station 2 in the steel fiber concrete construction area, as shown in Figure 12a. Surface displacement of the roadway is monitored by the "cross-point method". A measuring point is arranged at the center of the roof plate (A), the center of the bottom plate (B), the center of the left gang (C), the center of the backfill body (D), and the laser range finder is used to monitor the displacement change between AB and CD at regular intervals. Use the bolt (cable) force measuring agent to monitor the force of the bolt (cable); the bolt monitoring number is B1~B6, and the cable number is C1~C2. The arrangement of the road surface displacement and the bolt (cable) axial force monitoring is shown in Figure 12b,c.

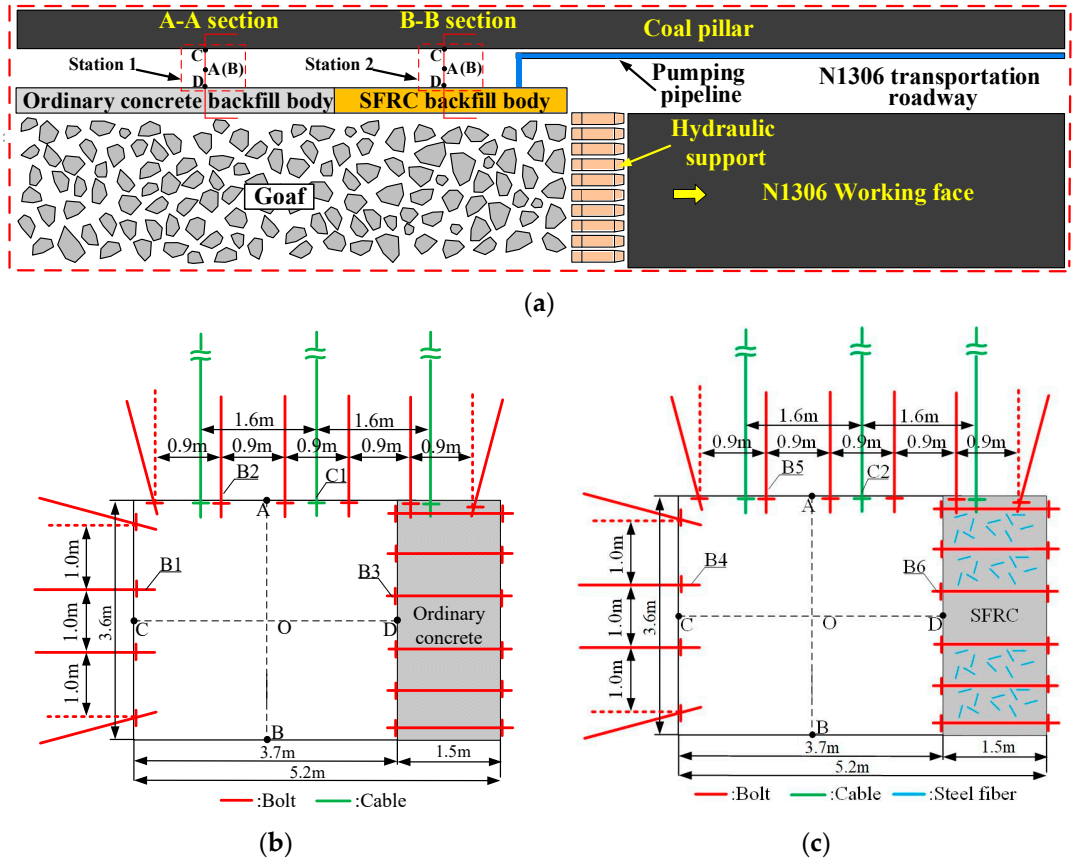


Figure 12. Monitoring station layout and monitoring section: (**a**) Monitoring station layout; (**b**) A-A section; (**c**) B-B section.

4.3.2. Monitoring Results

The displacement of the roadway surface and the force on the bolt (cable) are shown in Figure 13.

As shown in Figure 13a,b, when the working face is ahead of the measuring station by 0–20 m, the surface deformation of the roadway is relatively small. When the working face is ahead of the measuring station by 20–60 m, the subsidence of the roof and the displacement of the two sides continue to increase, and the deformation of the surrounding rock significantly increases. When the working face is ahead of the measuring station by about 70 m, the deformation of the roadway gradually tends to stabilize, and the deformation of the SFRC roadway area is significantly smaller than that of the ordinary concrete roadway area. The maximum displacement of the top and bottom plates measured by Station 1 is 297 mm, and the maximum displacement of the two sides is 224 mm. The maximum displacement of the top and bottom plates measured at Station 2 is 198 mm, and the maximum displacement of the two sides is 152 mm. Compared with Station 1, the

displacement of the top and bottom plates and the displacement of the two sides of Station 2 have decreased by 33.33% and 32.14%, respectively. The deformation of the roadway in the SFRC roadway area has been effectively improved.

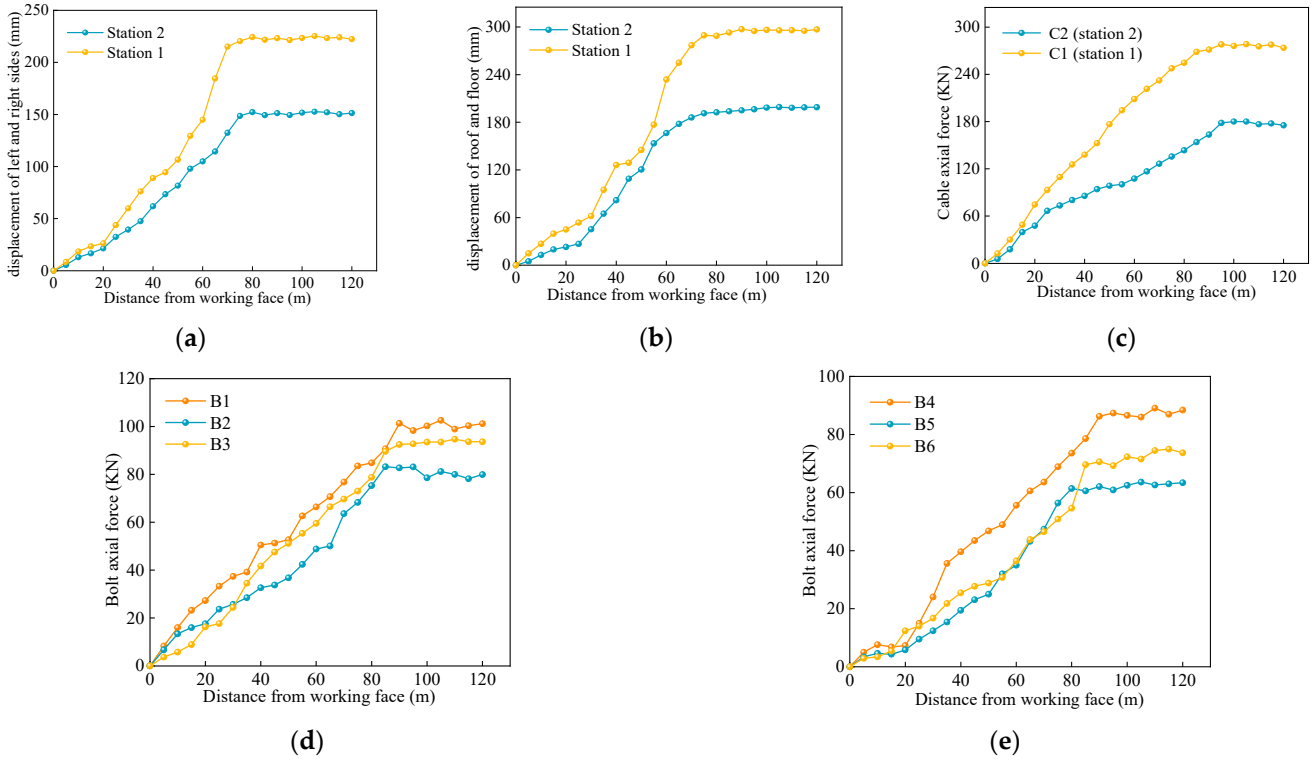


Figure 13. Surface displacement and change in axial force of bolt (cable): (**a**) Left-right gang displacement; (**b**) roff-floor plate displacement; (**c**) cable axial force change; (**d**) bolt axial force change of Station 1; (**e**) bolt axial force change of Station 2.

The variation of axial force of bolts (cables) is roughly the same as the pattern exhibited by the deformation of the tunnel surface and can also be roughly divided into three stages. From Figure 13c–e, it can be seen that the maximum axial forces of anchor rods B1, B2, and B3 in Station 1 are 102.6 KN, 94.7 KN, and 83.2 KN, respectively, and the maximum axial force of the anchor cable is 277.7 KN. The maximum axial forces of anchor rods B4, B5, and B6 in Station 2 are 89.1 KN, 75 KN, and 63.6 KN, respectively, and the maximum axial force of the anchor cable is 178.3 KN. Compared with Station 1, the B4, B5, and B6 bolts and cable axial forces of Station 2 have decreased by 13%, 20%, 23%, and 35%, respectively.

5. Discussion

It is evident that using SFRC as a roadside backfill material can effectively reduce roadway surface deformation and force on the bolt (cable) while also addressing issues such as cracking of the flexible mold package and instability of the backfill body. SFRC enhances roadway stability and safety, enriching the variety of roadside filling materials and promoting the use of steel fiber concrete. However, this paper does not explore the use of other types of steel fibers and their effectiveness in coal mines. It is important to note that different types of steel fibers have varying mobility and toughening effects, which require further research and discussion. Additionally, the cost of steel fiber must also be considered when used in coal mines.

6. Conclusions

Through the meticulous examination and analysis of SFRC slump and mechanical properties, a high-strength and high-toughness roadside backfill material suitable for coal

mines was procured. Subsequently, an engineering application was executed in a Shanxi mine, leading to the derivation of the following conclusions:

1. The slump of concrete decreases with the increase of steel fibers. Considering factors such as pumping distance, it is determined that the amount of steel fiber added on site should be between 0.5% and 1.5%.
2. The inclusion of steel fiber shifts the three stages of pore compaction, linear elasticity, and instability damage in the stress–strain curve forward. It also causes the residual stage curve of the post-peak stage to step down, resulting in a stronger post-peak bearing capacity.
3. The compressive and tensile strengths of concrete showed an increasing and then decreasing trend with the increase of steel fibers, reaching the peak at 1.5%, and the steel fibers were more obvious for tensile strength enhancement. Steel fibers enhance the strength of compressive strength of concrete at an early age, weaker at a late age, and tensile strength inversely.
4. The incorporation of steel fibers reduces the degree of damage to the concrete matrix and changes the concrete matrix from tensile to shear damage. Relevant calculations show that the toughness index of steel fiber concrete exhibits a 'first increase and then decrease' trend, with the maximum toughness index achieved at a mixing amount of 1.5%.
5. The industrial test results demonstrate that using SFRC as the filling material for roadside structures can effectively reduce peripheral rock surface displacement and bolt (cable) force. This proves the feasibility of using SFRC as roadside filling material.

Author Contributions: Conceptualization, X.Z. and X.S.; Formal analysis, X.L.; Funding acquisition, X.S. and J.N.; Methodology, J.N.; Visualization, Y.L. and S.Y.; Writing—original draft, X.Z. and X.S.; Writing—review and editing, X.L. All authors have read and agreed to the published version of the manuscript.

Funding: This study received assistance from the National Natural Science Foundation of China (Nos. 52204100, 52374130, 52074170).

Data Availability Statement: The data presented in this study are available on request from the corresponding author.

Conflicts of Interest: The authors declare no conflicts of interest.

References

1. Zhang, X. Surrounding Rock Control Mechanism and Application of "Support-Unloading" Combined Technology for Gob-SideEntry Retaining in Shallow Coal Seam. Ph.D. Thesis, China Coal Research Institute, Xi'an, China, 2022. [CrossRef]
2. Kang, H.; Zhang, X.; Wang, D.; Tian, J.; Yi, Z.; Jiang, W. Strata control technology and applications of non-pillar coal mining. *J. China Coal Soc.* **2022**, *47*, 16–44. [CrossRef]
3. Sun, X.; Zhang, L.; Zhang, B. Research on the coal industry development and transition in China under the background ofcarbon neutrality. *China Min. Mag.* **2021**, *30*, 1–6. [CrossRef]
4. Zhang, S. Coordinate and push industry energy-saving and carbon reduction, actively deal with carbon peak, and carbon neutrality challenge. *Coal Process. Compr. Util.* **2021**, *5*, 1–6. [CrossRef]
5. Wang, Q.; He, M.; Yang, J.; Gao, H.; Jiang, B.; Yu, H. Study of a no-pillar mining technique with automatically formed gob-side entry retaining for longwall mining in coal mines. *Int. J. Rock. Mech. Min. Sci.* **2018**, *110*, 1–8. [CrossRef]
6. Luan, H.; Jiang, Y.; Zhou, L.; Lin, H. Stability Control and Quick Retaining Technology of Gob-Side Entry: A Case Study. *Adv. Civ. Eng.* **2018**, *2018*, 7357320. [CrossRef]
7. Hou, C. Key technologies for surrounding rock control in deep roadway. *J. China Univ. Min. Technol.* **2017**, *46*, 970–978. [CrossRef]
8. Zhang, Z.; Bai, J.; Chen, Y.; Yan, S. An innovative approach for gob-side entry retaining in highly gassy fully-mechanized longwall top-coal caving. *Int. J. Rock. Mech. Min. Sci.* **2015**, *80*, 1–11. [CrossRef]
9. Li, Q.; Xu, S. Performance and application of ultra high toughness cementitious composite:aeview. *Eng. Mech.* **2009**, *26*, 23–67.
10. Xu, S.; Zhang, Z.; Xin, J.; Bai, J.; Ma, X.; Zhai, R.; Wu, W. Stability mechanism and countermeasure of the solid coal rib in deep gob-side entry retaining: Insights from theoretical analysis numerical simulation. *Heliyon* **2024**, *10*, e24174. [CrossRef]
11. Hua, X.; Li, C.; Liu, X.; Guo, Y.; Qi, Y.; Chen, D. Current situation of gob-side entry retaining and suggestions for its improvement in China. *Coal Sci. Technol.* **2023**, *51*, 128–145. [CrossRef]

12. Xie, S.-R.; Pan, H.; Chen, D.-D.; Zeng, J.-C.; Song, H.-Z.; Cheng, Q.; Xiao, H.-B.; Yan, Z.-Q.; Li, Y.-H. Stability analysis of integral load-bearing structure of surrounding rock of gob-side entry retention with flexible concrete formwork. *Tunn. Undergr. Space Technol.* **2020**, *103*, 103492. [CrossRef]
13. Li, V.C.; Wu, H.C.; Maalej, M.; Mishra, D.K.; Hashida, T. Tensile Behavior of Cement-Based Composites with Random Discontinuous Steel Fibers. *J. Am. Ceram. Soc.* **2005**, *79*, 74–78. [CrossRef]
14. Li, V.C.; Obla, K.H. Effect of fiber length variation on tensile properties of carbon-fiber cement composites. *Compos. Eng.* **1994**, *4*, 947–964. [CrossRef]
15. Wansom, S.; Janjaturaphan, S. Evaluation of fiber orientation in plant fiber-cement composites using AC-impedance spectroscopy. *Cem. Concr. Res.* **2013**, *45*, 37–44. [CrossRef]
16. Khan, S.; Ashraf, S.; Ali, S.; Khan, K. Experimental investigations on the mechanical properties and damage detection of carbon nanotubes modified crumb rubber concrete. *J. Build. Eng.* **2023**, *75*, 106937. [CrossRef]
17. Al-Akhras, N.M.; Smadi, M.M. Properties of tire rubber ash mortar. *Cem. Concr. Compos.* **2004**, *26*, 821–826. [CrossRef]
18. Khaloo, A.R.; Dehestani, M.; Rahmatabadi, P. Mechanical properties of concrete containing a high volume of tire-rubber particles. *Waste Manag.* **2008**, *28*, 2472–2482. [CrossRef] [PubMed]
19. Li, G.; Shi, X.; Gao, Y.; Ning, J.; Chen, W.; Wei, X.; Wang, J.; Yang, S. Reinforcing effects of carbon nanotubes on cement-based grouting materials under dynamic impact loading. *Constr. Build. Mater.* **2023**, *382*, 131083. [CrossRef]
20. Li, G.; Shi, X.; Ning, J.; Chen, W.; Zhang, Z.; Wang, J.; Yang, S.; Gao, Y. Particle size distribution of aggregate effects on the dynamic compressive behavior of cement waste rock backfill. *Eng. Fract. Mech.* **2023**, *292*, 109596. [CrossRef]
21. Eftekhari, M.; Mohammadi, S. Multiscale dynamic fracture behavior of the carbon nanotube reinforced concrete under impact loading. *Int. J. Impact Eng.* **2016**, *87*, 55–64. [CrossRef]
22. Ashwini, B. Comparison of mechanical properties of concrete incorporated with Multiwalled Carbon nanotube and partial replacement of cement with flyash. *Mater. Today Proc.* **2023**. [CrossRef]
23. Wang, Y.; Huang, H.; Zeng, J.; Hu, W.; Cheng, Y. Axial compressive behavior of recycled ceramic coarse aggregate concrete-filled steel tubular columns. *J. Constr. Steel Res.* **2023**, *210*, 108040. [CrossRef]
24. López, V.; Llamas, B.; Juan, A.; Morán, J.M.; Guerra, I. Eco-efficient Concretes: Impact of the Use of White Ceramic Powder on the Mechanical Properties of Concrete. *Biosyst. Eng.* **2007**, *96*, 559–564. [CrossRef]
25. Binici, H. Effect of crushed ceramic and basaltic pumice as fine aggregates on concrete mortars properties. *Constr. Build. Mater.* **2007**, *21*, 1191–1197. [CrossRef]
26. Roumaldi, J.P.; Batson, G.B. Mechanics of Crack Arrest in Concrete. *Proc. ASCE* **1963**, *89*, 147–168. [CrossRef]
27. Romualdi, J.P.; Mandel, J.A. Tensile Strength of Concrete Affected by Uniformly Distributed and Closely Spaced Short Lengths of Wire Reinforcement. *J. Proc.* **1964**, *61*, 27–37.
28. Lankard, D.R.; Newell, J.K. Preparation of Highly Reinforced Steel Fiber Reinforced Concrete Composites. *Spec. Publ.* **1984**, *81*, 287–306.
29. Naaman, A.E.; Homrich, J.R. Tensile stress-strain Properties of SIFCON. *ACI Mater. J.* **1989**, *86*, 244–251.
30. Li, V.C.; Leung, C. Steady-State and Multiple Cracking of Short Random Fiber Composites. *ASCE* **1992**, *118*, 2246–2264. [CrossRef]
31. Khaloo, A.; Kim, N. Mechanical properties of normal to high-strength steel fiber-reinforced concrete. *Cem. Concr. Aggreg.* **1996**, *18*, 92–97. [CrossRef]
32. Wang, Z.; Li, H.; Zhang, X.; Chang, Y.; Wang, Y.; Wu, L.; Fan, H. The Effects of Steel Fiber Types and Volume Fraction on the Physical and Mechanical Properties of Concrete. *Coatings* **2023**, *13*, 978. [CrossRef]
33. Meng, S.; Jiao, C.; Ouyang, X.; Niu, Y.; Fu, J. Effect of steel fiber-volume fraction and distribution on flexural behavior of Ultra-high performance fiber reinforced concrete by digital image correlation technique. *Constr. Build. Mater.* **2022**, *320*, 126281. [CrossRef]
34. Luo, Z.; Li, X.; Ling, T. Study on the Reinforcement Mechanism and Fracture Mechanics Model of Steel Fiber Reinforced Concrete. *Min. Res. Dev.* **2003**, *23*, 18–22. [CrossRef]
35. Sun, W.; Gao, J.; Qin, H. Studies on bond strength of inter face between fiber and matrix steel fiber reinforced concrete. *J. Chin. Ceram. Soc.* **1985**, *13*, 292–300.
36. Rashidi, M.; Kargar, S.; Roshani, S. Experimental and numerical investigation of steel fiber concrete fracture energy. In *Structures*; Elsevier: Amsterdam, The Netherlands, 2024; Volume 59, p. 105792. [CrossRef]
37. Nguyen, K.T.Q.; Navaratnam, S.; Mendis, P.; Zhang, K.; Barnett, J.; Wang, H. Fire safety of composites in prefabricated buildings: From fibre reinforced polymer to textile reinforced concrete. *Compos. Part. B Eng.* **2020**, *187*, 107815. [CrossRef]
38. Lárusson, L.H.; Fischer, G.; Jönsson, J. Prefabricated floor panels composed of fiber reinforced concrete and a steel substructure. *Eng. Struct.* **2013**, *46*, 104–115. [CrossRef]
39. Teng, J.G.; Yu, T.; Fernando, D. Strengthening of steel structures with fiber-reinforced polymer composites. *J. Constr. Steel Res.* **2012**, *78*, 131–143. [CrossRef]
40. *DG/TJ08-59-2019*; Technical Specification for Application of Mill-Cut Steel Fiber Reinforced Concrete. Tongji University Press: Shanghai, China, 2019.
41. *JGJ 55-2011*; Specification for Mix Proportion Design of Ordinary Concrete. China Architecture & Building Press: Beijing, China, 2011.
42. *JG/T472-2015*; Steel Fiber Reinforced Concrete. Ministry of Housing and Urban Rural Development of the People's Republic of China: Beijing, China, 2015.

43. Ashkezari, G.D.; Fotouhi, F.; Razmara, M. Experimental relationships between steel fiber volume fraction and mechanical properties of ultra-high performance fiber-reinforced concrete. *J. Build. Eng.* **2020**, *32*, 101613. [CrossRef]
44. Soufeiani, L.; Raman, S.N.; Jumaat, M.Z.B.; Alengaram, U.J.; Ghadyani, G.; Mendis, P. Influences of the volume fraction and shape of steel fibers on fiber-reinforced concrete subjected to dynamic loading—A review. *Eng. Struct.* **2016**, *124*, 405–417. [CrossRef]
45. Lu, X.; Zhang, Y.; Zhang, H.; Zhang, H.; Xiao, R. Experimental study on seismic performance of steel fiber reinforced high strength concrete composite shear walls with different steel fiber volume fractions. *Eng. Struct.* **2018**, *171*, 247–259. [CrossRef]
46. *GB/T 50080-2016*; Standard for Test Method of Performanceon Ordinary Fresh Concrete. China Architecture & Building Press: Beijing, China, 2016.
47. *ASTM-C143*; Standard Test Method for Slump of Hydraulic-Cement Concrete. American Society of Testing Materials: Philadelphia, PA, USA, 2020.
48. *GB/T 50081-2019*; Standard for Test Methods of Concrete Physical and Mechanical Properties. China Architecture & Building Press: Beijing, China, 2019.
49. *ASTM-C39*; Standard Test Method for Compressive Strength of Cylindrical Concrete Specimens. American Society of Testing Materials: Philadelphia, PA, USA, 2018.
50. *ASTM-C496*; Splitting Tensile Strength of Cylindrical Concrete Specimens. American Society of Testing Material: Philadelphia, PA, USA, 2017.
51. Boulekbache, B.; Hamrat, M.; Chemrouk, M.; Amziane, S. Flowability of fiber-reinforced concrete and its effect on the mechanical properties of the material. *Constr. Build. Mater.* **2010**, *24*, 1664–1671. [CrossRef]
52. Yu, J.; Zhai, T.; Liang, X.; Sun, X. Fluidity and Mechanical Properties of Steel-PVA Fiber Reinforced Concrete. *J. Build. Mater.* **2018**, *21*, 402–407.
53. *JGJ/T 10-2011*; Technical Specification for Construction of Concrete Pumping. China Architecture & Building Press: Beijing, China, 2011.
54. Zhang, Z.; Zhang, D.; Zhang, X. Experimental study on "soft-carrying" of mine concrete support material. *Concrete* **2022**, *10*, 179–183.
55. Bai, M.; Niu, H.; Jiang, L.; Miao, Y. Research on Improving the Mechanical Properties andMicrostructure of Concrete with Steel Fiber. *Bull. Chin. Ceram. Soc.* **2013**, *32*, 2084–2089. [CrossRef]
56. Park, S.H.; Kim, D.J.; Ryu, G.S.; Koh, K.T. Tensile behavior of Ultra High Performance Hybrid Fiber Reinforced Concrete. *Cem. Concr. Compos.* **2012**, *34*, 172–184. [CrossRef]
57. Yang, X.X.; Sun, D.K.; Jing, H.W. Morphological features of shear-formed fractures developed in a rock bridge. *Eng. Geol.* **2020**, *278*, 105833. [CrossRef]
58. Xie, H.; Peng, R.; Ju, Y.; Zhou, H. On energy analysis of rock failure. *Chin. J. Rock. Mech. Eng.* **2005**, *24*, 2603–2608.
59. Fu, Q.; Zhao, X.; He, J.; Zhang, Z.; Zeng, X.; Niu, L.; Wang, Y. Constitutive Response of Hybrid Basalt-polypropylene Fiber-reinforced Concrete Based on Energy Conversion Principle. *J. Chin. Ceram. Soc.* **2021**, *49*, 1670–1682. [CrossRef]
60. Zhao, C.; Zhu, Z.; Guo, Q.; Zhan, Y.; Zhao, R. Research on fiber reinforced concrete and its performance prediction method and mix design method. *Constr. Build. Mater.* **2023**, *365*, 130033. [CrossRef]
61. Wang, X. Study on the Bond Mechanism of Deformed Steel Fiber and Concrete and Toughening Effect. Master's Thesis, Hebei University of Technology, Tianjin, China, 2003.
62. Huo, L. The Constitutive Model and Numerical Analysis of the Steel Fiber Reinforcement Concrete Based on the Smear Crack Model. Ph.D. Thesis, Tianjin University, Tianjin, China, 2023.

Disclaimer/Publisher's Note: The statements, opinions and data contained in all publications are solely those of the individual author(s) and contributor(s) and not of MDPI and/or the editor(s). MDPI and/or the editor(s) disclaim responsibility for any injury to people or property resulting from any ideas, methods, instructions or products referred to in the content.